Description of plastic anisotropy in AA6063-T6 using the crystal plasticity finite element method

4 authors:

Stephane Dumoulin
SINTEF
65 PUBLICATIONS   1,391 CITATIONS

SEE PROFILE

Olaf Engler
Speira GmbH
222 PUBLICATIONS   6,632 CITATIONS

SEE PROFILE

Odd Sture Hopperstad
Norwegian University of Science and Technology
379 PUBLICATIONS   13,315 CITATIONS

SEE PROFILE

Odd-Geir Lademo
SINTEF
65 PUBLICATIONS   1,409 CITATIONS

SEE PROFILE

Some of the authors of this publication are also working on these related projects:

Project   Impact against offshore pipelines View project

Project   FractAl View project

Description of plastic anisotropy in AA6063-T6 using the crystal plasticity finite element method

Description of plastic anisotropy in AA6063-T6 using the crystal plasticity finite element method

S Dumoulin[1,3], **O Engler**[2,3], **O S Hopperstad**[3,4] **and O G Lademo**[1,3,4]

[1] SINTEF Materials and Chemistry, NO-7465 Trondheim, Norway
[2] Hydro Aluminium Rolled Products GmbH, R&D Center Bonn, PO Box 2468, D-53014 Bonn, Germany
[3] Structural Impact Laboratory (SIMLab), Centre for Research-based Innovation, NO-7491 Trondheim, Norway
[4] Department of Structural Engineering, Norwegian University of Science and Technology, NO-7491 Trondheim, Norway

Abstract

The crystal plasticity finite element method has been used in combination with crystallographic texture data to predict the plastic anisotropy of the extruded aluminium alloy AA6063 in temper T6. The results are compared with experimental data from tensile tests at different angles between the tensile and extrusion directions. Inverse modelling based on the tensile test in a reference direction is used to identify the parameters of the work-hardening model at slip system level. To investigate the influence of grain interactions, various discretizations of the grains are applied in the representative volume element modelled with finite elements. In addition, alternative homogenization schemes, such as the full-constraint Taylor and viscoplastic self-consistent methods, are used to model the behaviour of the polycrystal. It is found that the grain discretization and the homogenization scheme have only minor influence on the predicted plastic anisotropy. While the crystal plasticity-based methods all give reasonable predictions of the directional variations of flow stresses and plastic strain ratios measured experimentally, there are still significant deviations, indicating there are other sources to the plastic anisotropy than crystallographic texture.

(Some figures may appear in colour only in the online journal)

1. Introduction

Today, it is well established that the mechanical properties of sheets and extrusions of aluminium alloys are strongly correlated with the final microstructure and crystallographic texture, which in turn depend on the thermo-mechanical process history of the product [1]. In extrusion, production of profiles involves several processing steps, where the actual extrusion

process has a determinant role on the final properties of the product and typically induces strong anisotropy in plastic properties [2–11].

Numerous phenomenological models and yield criteria have been developed through the years to describe plastic anisotropy in metals [12–19]. Among these, the anisotropic Yld2004-18p yield function proposed by Barlat *et al* [19] has proven good capabilities in reproducing accurately experimental data for different aluminium alloys [10, 11]. In a recent study, some of the present authors used the Yld2004-18p yield function together with a non-linear isotropic work-hardening rule to describe plastic anisotropy in flat profiles from the two alloys AA6063-T6 and AA7003-T6 [11]. Significant deviations between predicted and experimental results were revealed and attributed to the parameter identification procedure and to the assumption of isotropic hardening, which was shown to be inadequate due to important texture evolution. It was also shown that the parameter identification procedure plays a significant role in the quality of the results.

It may be argued that such a phenomenological approach is rather costly since it requires execution of a large number of experimental tests and provides no physical understanding of the observed phenomena, e.g. insight into the texture evolution responsible for changes in plastic anisotropy during plastic deformation.

A complementary procedure, which is currently gaining momentum, is to use a top–down approach where lower-scale models are built and used for calibration of phenomenological upper-scale models (e.g. [30, 31]). An advanced, and nowadays rather common approach is the use of crystal plasticity. The combination of crystal plasticity with the finite element method, or CP-FEM, has gained increasing interest over the last ten to fifteen years and has proven being reliable [20–31]. A recent extensive review on CP-FEM describes this approach, its applications and its challenges [32]. In CP-FEM, the grains are explicitly resolved together with their crystallographic orientation. The initial texture of the material under study as well as its evolution can therefore be accounted for. Hardening is modelled at the slip system level and the global, or macroscopic, behaviour thus originates from interactions between slip systems within grains combined with inter-granular interactions.

Previous studies on description of plastic anisotropy in aluminium using crystal plasticity-based approaches have been performed by several authors (e.g. [8, 30–34, 51]). The approaches utilized are either so-called grain interaction models, i.e. modified Taylor-type homogenization, or two-dimensional CP-FEM, three-dimensional CP-FEM being scarcely used. These studies show that models which take grain interactions into account are more successful in reproducing the experimental trends. However, comparisons between the different approaches on specific industrial alloys are necessary to evaluate the different approaches but are scarce.

This study aims at describing plastic anisotropy in aluminium alloy AA6063-T6 by use of CP-FEM using a simple but computationally efficient approach. A representative volume element (RVE) is chosen to describe the material under study. A Voce-type hardening model written at the slip system level is calibrated using experimental data from a single tensile test. The RVE is then subjected to loading in different directions from which plastic anisotropy is obtained.

This paper is organized as follows. Section 2 describes the rate-dependent constitutive model used at the crystal level. Section 3 summarizes the main experimental facts of relevance for this study. The modelling methodology, i.e. choice and discretization of a RVE and associated texture using CP-FEM, is described in section 4. The main numerical results, comparisons against experimental data and assessments of the effects from texture and grain discretization are presented in section 5. Section 6 compares different polycrystal modelling approaches. In the last section before the conclusion, the results are discussed and the weaknesses of the approach are identified.

2. Rate-dependent model for single crystals

2.1. Kinematics and kinetics

The formulation chosen in this study relies on the multiplicative decomposition of the total deformation gradient $\boldsymbol{F}$ into an inelastic component $\boldsymbol{F}^{\mathrm{p}}$, corresponding to the plastic flow of matter through the lattice by slip-induced shearing, and an elastic component $\boldsymbol{F}^{\mathrm{e}}$, associated with elastic stretching and rigid body rotation of the crystal lattice, as initially suggested by Lee and Liu [35] and Mandel [36] and used by many authors in the context of crystal plasticity [20–30]. The total deformation gradient $\boldsymbol{F}$ reads

$$\boldsymbol{F} = \boldsymbol{F}^{\mathrm{e}} \boldsymbol{F}^{\mathrm{p}} \tag{1}$$

where $\det(\boldsymbol{F}) = \det(\boldsymbol{F}^{\mathrm{e}})$ or $\det(\boldsymbol{F}^{\mathrm{p}}) = 1$, i.e. plastic incompressibility is assumed.

The plastic velocity gradient $\overline{\boldsymbol{L}}^{\mathrm{p}}$ in the intermediate configuration, due to crystallographic slip, is the plastic part of the total velocity gradient pulled-back from the current to the intermediate configuration. Since plastic deformation is caused by dislocation slip on slip systems, it can be shown that [37]

$$\overline{\boldsymbol{L}}^{\mathrm{p}} = \dot{\boldsymbol{F}}^{\mathrm{p}} \boldsymbol{F}^{\mathrm{p}-1} = \sum_{\alpha=1}^{n} \dot{\gamma}^{\alpha} \boldsymbol{m}_0^{\alpha} \otimes \boldsymbol{n}_0^{\alpha} \tag{2}$$

where $\boldsymbol{m}_0^{\alpha}$ and $\boldsymbol{n}_0^{\alpha}$ are unit vectors defining the slip direction and slip plane normal, respectively, for the slip system α and $\dot{\gamma}^{\alpha}$ the slip rate of slip system α measured relative to the undeformed lattice; n is the total number of active slip systems in the crystal. Note that plastic slip, or $\boldsymbol{F}^{\mathrm{p}}$, does not affect $\boldsymbol{m}_0^{\alpha}$ and $\boldsymbol{n}_0^{\alpha}$. For faced centred cubic (fcc) metals, slip occurs on the twelve $\{1\,1\,1\}\langle 1\,1\,0\rangle$ slip systems.

The intermediate configuration represents a reference configuration for the elastic part of the deformation, i.e. the elastic strains are measured with respect to the intermediate configuration. The elastic response is defined by an elastic stored energy potential, assuming small elastic strains and a quadratic potential in terms of the elastic Green strain on the intermediate configuration. The second Piola–Kirchhoff stress thus reads

$$\overline{\boldsymbol{S}}^{\mathrm{e}} = \overline{\boldsymbol{K}}^{\mathrm{e}} : \overline{\boldsymbol{E}}^{\mathrm{e}} \tag{3}$$

with

$$\overline{\boldsymbol{E}}^{\mathrm{e}} = \tfrac{1}{2}(\boldsymbol{F}^{\mathrm{eT}} \boldsymbol{F}^{\mathrm{e}} - \boldsymbol{I}) = \tfrac{1}{2}(\overline{\boldsymbol{C}}^{\mathrm{e}} - \boldsymbol{I}) \tag{4}$$

and

$$\overline{\boldsymbol{S}}^{\mathrm{e}} = \det(\boldsymbol{F})(\boldsymbol{F}^{\mathrm{e}-1} \boldsymbol{\sigma} \boldsymbol{F}^{\mathrm{e}-\mathrm{T}}) \tag{5}$$

where $\overline{\boldsymbol{K}}^{\mathrm{e}}$ is the fourth order tensor of elastic constants, $\overline{\boldsymbol{C}}^{\mathrm{e}}$ is the elastic right Cauchy–Green deformation tensor and $\boldsymbol{\sigma}$ is the symmetric Cauchy stress tensor.

The total power per unit reference volume of the crystal can be defined as the additive decomposition into elastic and plastic parts as

$$\dot{\omega} = \dot{\omega}^{\mathrm{e}} + \dot{\omega}^{\mathrm{p}} = \overline{\boldsymbol{S}}^{\mathrm{e}} : \dot{\overline{\boldsymbol{E}}}^{\mathrm{e}} + (\overline{\boldsymbol{C}}^{\mathrm{e}} \overline{\boldsymbol{S}}^{\mathrm{e}}) : \overline{\boldsymbol{L}}^{\mathrm{p}}. \tag{6}$$

Furthermore, the resolved shear stress, or the so-called generalized Taylor–Schmid stress, τ^{α}, acting on slip system α in the undeformed lattice is defined as the work conjugate to the slip rate. The plastic power per unit volume thus reads

$$\dot{\omega}^{\mathrm{p}} = \sum_{\alpha=1}^{n} \tau^{\alpha} \dot{\gamma}^{\alpha}. \tag{7}$$

Finally, using the above equations, the resolved shear stress reads

$$\tau^\alpha = \overline{C}^{\mathrm{e}}\overline{S}^{\mathrm{e}} : (m_0^\alpha \otimes n_0^\alpha). \tag{8}$$

The rotation of the crystal lattice was accounted for by computing the elastic rigid body rotation from the elastic deformation gradient F^{e} by use of the polar decomposition theorem.

2.2. Constitutive model

The constitutive model chosen here is based on the classical rate-dependent power-law relation [20, 25] and a modified Voce hardening model [38, 39]. The latter was chosen for its physical underpinning and its capability of describing strain hardening in fcc metals [39, 40].

The slip rate on each slip system is defined by the power-law relation

$$\dot{\gamma}^\alpha = \dot{\gamma}_0 \left| \frac{\tau^\alpha}{\tau_{\mathrm{c}}^\alpha} \right|^{\frac{1}{m}} sgn(\tau^\alpha) \tag{9}$$

where τ_{c}^α is the critical resolved shear stress, and m and $\dot{\gamma}_0$ are material constants representing the microscopic strain rate sensitivity and the reference shearing rate, respectively. Note that the reference shearing rate could be different for each slip system.

Work-hardening is introduced by making the critical resolved shear stress a function of the plastic straining

$$\dot{\tau}_{\mathrm{c}}^\alpha = \theta(\Gamma) \sum_{\beta=1}^{n} q_{\alpha\beta} |\dot{\gamma}^\beta| \tag{10}$$

where θ defines the hardening rate for a given accumulated plastic strain and $q_{\alpha\beta}$ is the latent hardening matrix defined by

$$q_{\alpha\beta} = \begin{cases} 1 & \text{if } \alpha = \beta \\ q & \text{otherwise.} \end{cases} \tag{11}$$

Γ is the accumulated plastic shear strain defined by

$$\dot{\Gamma} = \sum_{\alpha=1}^{n} |\dot{\gamma}^\alpha|. \tag{12}$$

The work-hardening rate θ is defined as the derivative with respect to Γ of a master hardening curve in the form [39]

$$\tau_{\mathrm{c}}(\Gamma) = \tau_0 + (\tau_1 + \theta_1\Gamma)\left[1 - \exp\left(-\frac{\theta_0}{\tau_1}\Gamma\right)\right]. \tag{13}$$

Then, the work-hardening rate θ is calculated as

$$\theta(\Gamma) = \frac{\mathrm{d}\tau_{\mathrm{c}}(\Gamma)}{\mathrm{d}\Gamma} = \theta_1 + \left(\theta_0 - \theta_1 + \frac{\theta_0\theta_1}{\tau_1}\Gamma\right)\exp\left(-\frac{\theta_0}{\tau_1}\Gamma\right). \tag{14}$$

Here τ_0 and θ_0 are, respectively, the initial critical resolved shear stress and initial hardening rate, while θ_1 and τ_1 describe the asymptotic hardening.

There are altogether seven independent material parameters to be identified.

2.3. Time integration

The model described above has been implemented into the explicit non-linear finite element code LS-DYNA [41] by use of a user material subroutine (UMAT) developed for solid elements. The time integration of the model is performed using the fully explicit algorithm proposed by [26] based on an Euler-forward scheme. This scheme has proven being fast, accurate and robust for crystal plasticity simulations [42].
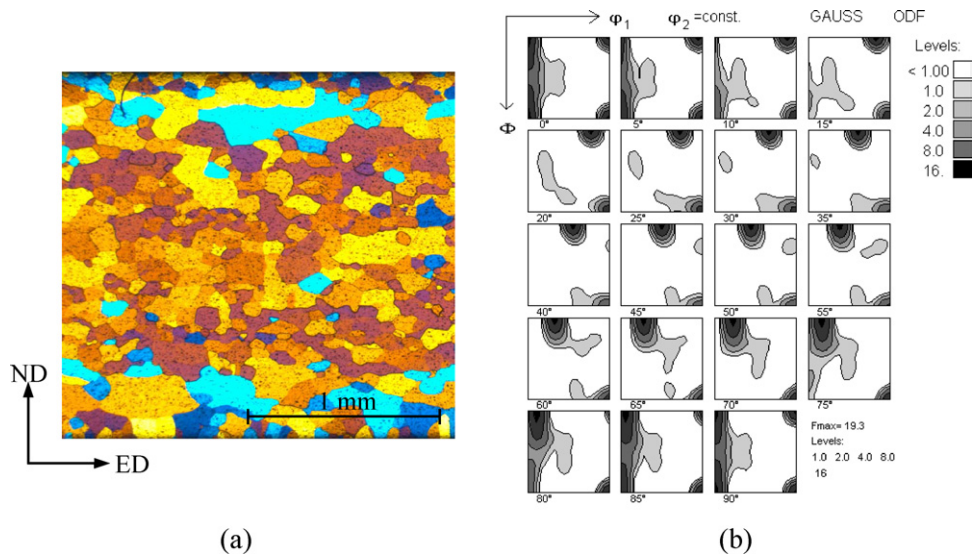
4

Figure 1. (*a*) Grain structure [10] and (*b*) ODF for AA6063-T6.

3. Experimental data

Only experimental details relevant for this study will be described hereafter. For more details, the reader is referred to the foregoing papers [10, 11].

The material studied in this work is aluminium alloy AA6063 (Iso Al Mg0.7 Si). It was received as flat extruded profile in temper T6 with a thickness of about 2 mm. The grain structure is recrystallized with equi-axed grains as shown in figure 1(*a*). The crystallographic texture was measured by electron back-scattered diffraction (EBSD). The measurements were performed from the transverse direction in the longitudinal section of the profile in order to take possible through-thickness texture variations into consideration. The EBSD data were then used to compute the orientation distribution function (ODF), shown in figure 1(*b*). The ODF reveals a typical recrystallization texture, i.e. a sharp cube texture with pronounced scatter about the extrusion direction (ED). The texture was also measured by standard x-ray diffraction techniques and compared with the one obtained by EBSD in order to compare the methods and validate the measurements [42]. Both methods gave similar results although the cube component was slightly higher when using x-rays.

Tensile test specimens with gauge length of 45 mm and width of 8 mm were machined from the extruded profile at seven angles, from $0°$ to $90°$ at $15°$ interval, with respect to the ED [10]. The obtained true stress versus true strain curves are shown in figure 2. Significant anisotropy both in strength and uniform strain is observed which is attributed to the strong texture of the material.
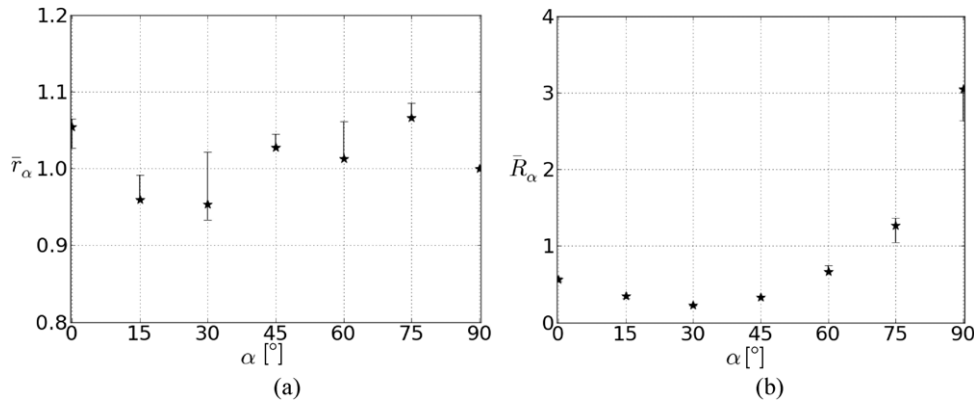
Directional flow stress ratios and plastic strain ratios were computed based on the true stress versus true strain curves. The flow stress ratio at a given plastic work is defined as

$$r_\alpha = \frac{\sigma_\alpha}{\sigma_{90}} \tag{15}$$

where σ_α is the flow stress in direction α and σ_{90} the flow stress in the transverse direction ($90°$), which is adopted here as a reference direction. The reason for this choice will be explained in
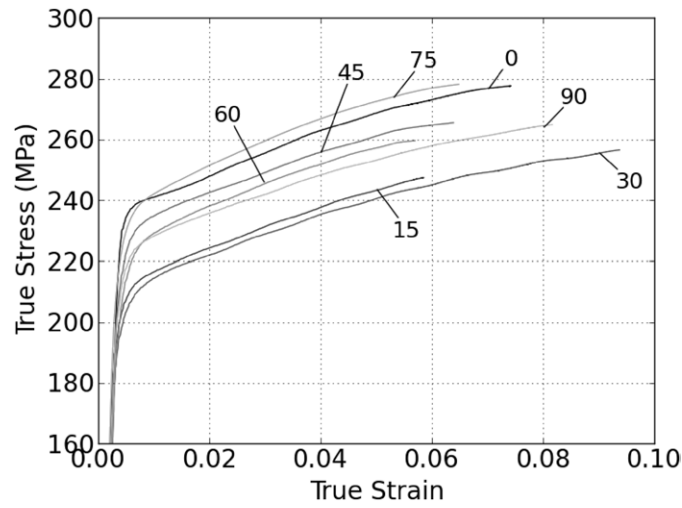
Figure 2. Experimental directional true stress versus true strain curves for AA6063-T6 up to onset of diffuse necking in the specimens.

Figure 3. Experimental directional (*a*) average flow stress ratio and (*b*) average plastic strain ratio.

section 4.2. The strain ratio, or *R*-value, is defined as

$$R_\alpha = \frac{\varepsilon_w^p}{\varepsilon_t^p} \tag{16}$$

where ε_w^p and ε_t^p are the plastic strains in width and thickness direction of the tensile specimen for direction α, respectively.

The obtained average flow stress ratio $\bar{r}_\alpha$ and average plastic strain ratio $\overline{R}_\alpha$ for plastic strains up to necking are shown in figure 3. In the experimental campaign, triplicate tests were performed in each direction. These tests revealed some variations, caused either by variations in material properties within the extrusion or in the test set-up itself. These variations are included in figure 3 as error bars for both average flow stress and average plastic strain ratios. The largest scatters are obtained in the 30°, 60° and 15° directions for the flow stress ratios and in the 75° and 90° directions for the plastic strain ratios.
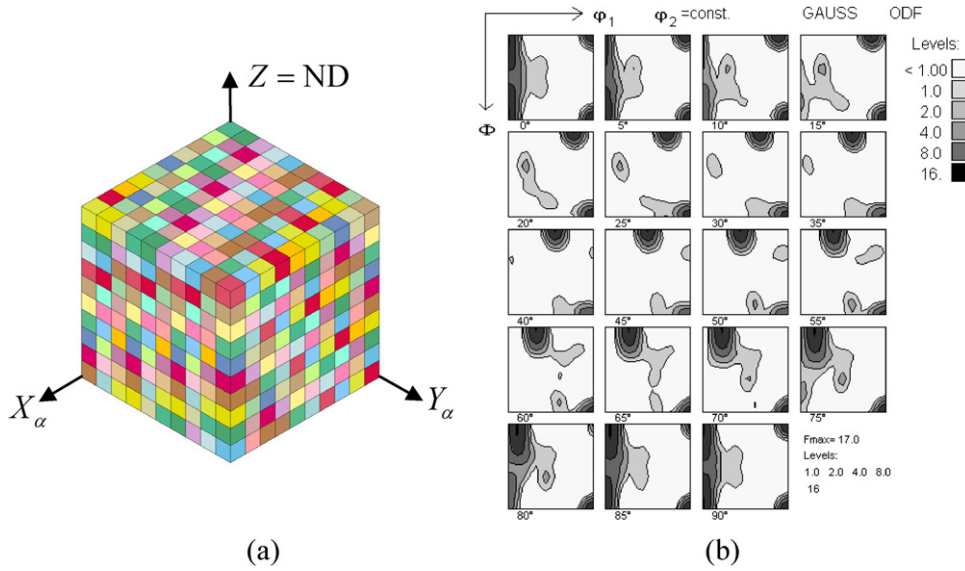
Figure 4. (*a*) RVE with 1000 grains and (*b*) model represented ODF.

4. Finite element modelling

4.1. Representative volume element

Based on the microstructural observations (see figure 1(*a*)), the material is considered as homogeneous in terms of both grain size and texture: except of the outer surface layers a constant grain size and a random spatial distribution of the texture components prevailed. Therefore, it is assumed that the material can be described using a CP-FEM RVE. As was shown in previous studies, 800 orientations are required to represent the material [44]. In this study a $2 \times 2 \times 2\,\text{mm}^3$ RVE made of $10 \times 10 \times 10$ grains is investigated using 1000 cubic eight-node elements with eight integration points (figure 4(*a*)). In other words, each grain is represented by only one finite element. A reduced texture made of 1000 orientations (figure 4(*b*)) was extracted from the measured one and orientations were assigned randomly to the elements of the RVE. In order to reproduce the experimental conditions during tensile testing, periodic boundary conditions were applied on the faces of the RVE orthogonal to the tensile X_α and transverse Y_α in-plane directions while the faces orthogonal to the normal direction (ND) were free (figure 4(*a*)).

To simulate tensile testing in different directions α with respect to the ED, the mesh and the boundary conditions remained fixed in space while the texture was rotated, i.e. the first Euler angle was increased by α. The frame associated with the RVE is thus (X_α, Y_α, Z) where X_α and Y_α are the tensile and transverse in-plane directions, respectively, of a tensile specimen located at an angle α from the ED and Z is the ND (figure 4(*a*)). Bunge's Euler angles are defined as φ_1 which rotates (X, Y, Z) into $(X', Y', Z' = Z)$ through a rotation about Z, Φ which rotates (X', Y', Z') into $(X'' = X', Y'', Z'')$ through a rotation about X' and φ_2 which rotates (X'', Y'', Z'') into $(X''', Y''', Z''' = Z'')$ through a rotation about Z''.

Table 1. Model parameters used in the simulations.

$\dot{\gamma}_0$ (s^{-1})	m	q	τ_0 (MPa)	θ_0 (MPa)	τ_1 (MPa)	θ_1 (MPa)
0.036	0.005	1.4	85.4	9.1×10^5	1.0	39.6

4.2. Calibration

Calibration of the model parameters was carried out with the design optimization tool LS-OPT [45] using the sequential response surface method with domain reduction together with a hybrid adaptive simulated annealing-leapfrog optimizer algorithm. Default settings were used. The parameters were identified only against the experimental curve for the 90° direction using the RVE described in the previous section. Prior trials based on a calibration against experimental curve for the 0° direction revealed difficulties for the CP-FEM approach in reproducing correctly the strength for the other directions.

In order to improve the efficiency of the calibration, some model parameters were identified from the literature. The microscopic strain rate sensitivity $1/m$ was set to 200 in order to represent the low strain rate sensitivity of the material under study; the latent hardening q was set to 1.4 as often used for fcc (e.g. [24, 26]); the reference shearing rate $\dot{\gamma}_0$ was set to 0.036. These parameters were then fixed in the calibration while the others were free. The values obtained after calibration are summarized in table 1. The elastic constants c_{11}, c_{12} and c_{44} were set to 106.43 GPa, 60.35 GPa and 28.21 GPa, respectively.

5. Results and comparisons with experiments

### 5.1. Comparisons with experiments

After calibration of the model parameters, simulations of tensile testing in all directions tested experimentally, i.e. from 0° to 90° at 15° interval, were run. Figure 5 compares the experimental and numerical results in terms of true stress versus true strain curves to onset of necking in the experimental test. Despite the difficulty in matching the sharp elastic–plastic transition, an almost perfect match is observed at 90° thus validating the calibration. Excellent agreements are also obtained at 30° and 45°, whereas deviations in strength up to ∼4%, 5%, 6% and 13% between experiments and simulations are observed at 75°, 15°, 60° and 0°, respectively.

5.2. Effect of texture discretization

The previous results were obtained using an RVE made of 1000 elements with a given spatial distribution of the texture. In order to assess the effect of the spatial distribution of the texture, two new different random assignments of the texture to the grains, or elements of the RVE, were generated. Thus, all together three different distributions, denoted 'texture 1000a', 'texture 1000b' and 'texture 1000c', were obtained. Furthermore, to validate the size of the RVE chosen, a new RVE made of 8000 grains using 8000 cubic eight-node elements was built. A reduced texture made of 8000 orientations was extracted from the measured one and assigned randomly to the elements of the RVE. Simulations were then run for each of these cases in all directions. The results obtained are shown in figure 6 for four selected orientations: 0°, 30°, 60° and 90° from the ED. Maximum deviations between the different texture discretizations are about 1%. This implies that the spatial distribution of the texture in the RVE has a negligible effect on the predicted work-hardening curves.
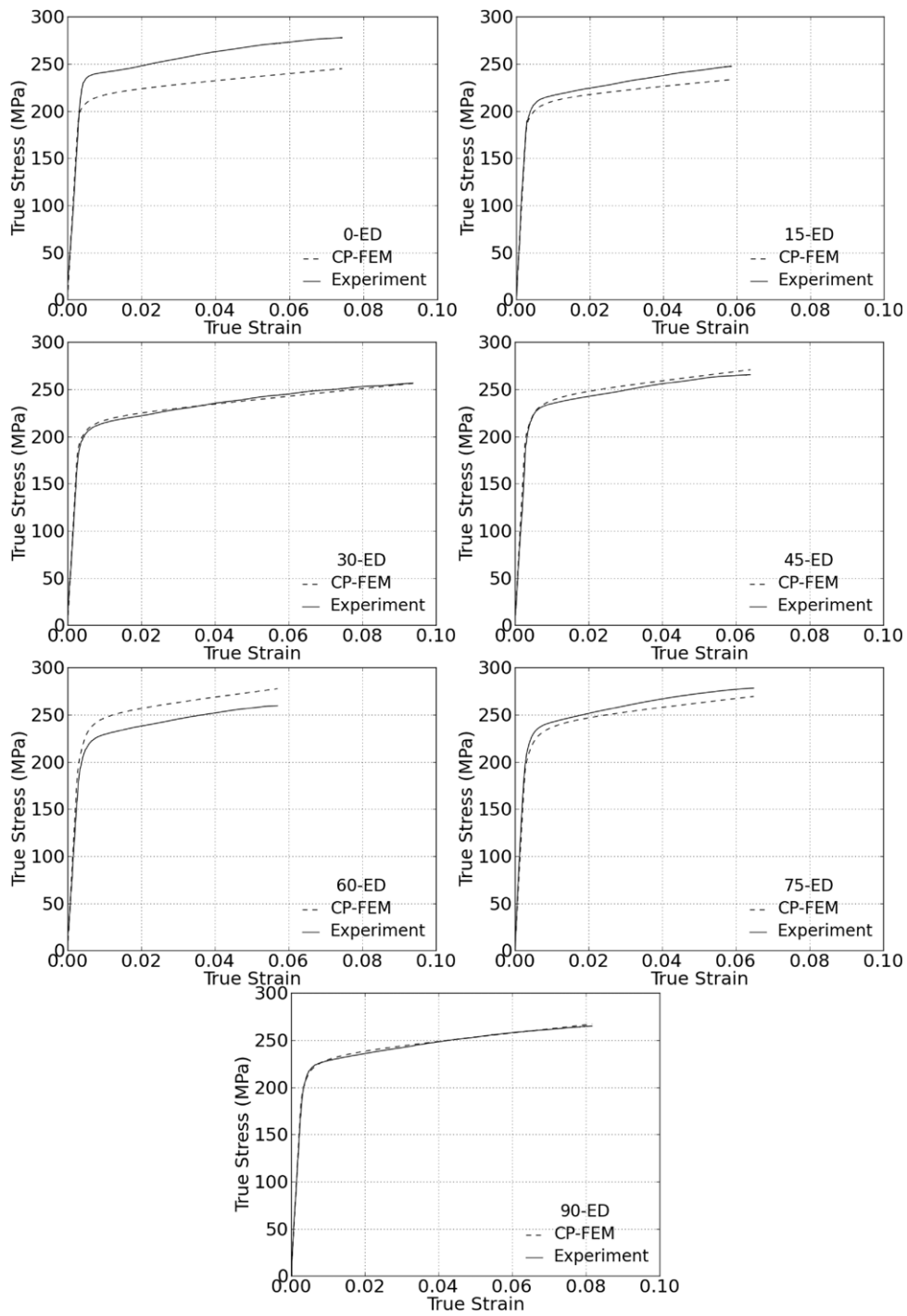
Figure 5. Comparison between experimental and numerical (CP-FEM) true stress versus true strain curves for each direction.
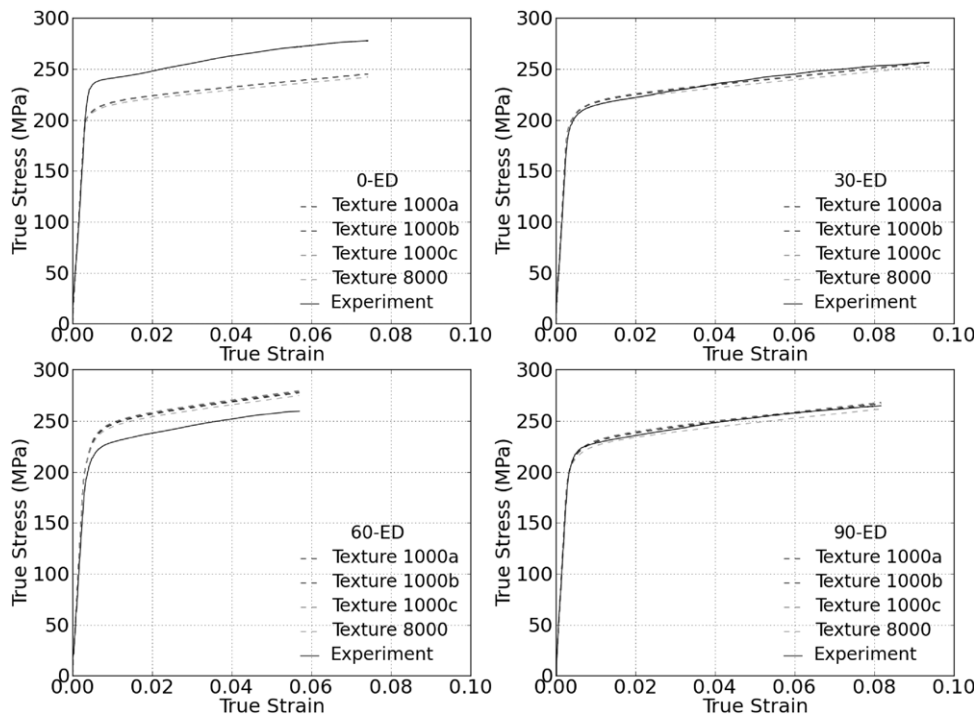
Figure 6. True stress versus true strain curves for 0°, 30°, 60° and 90° directions: comparison between experimental results and simulations for different RVEs.

Anisotropy in strength and plastic strain is characterized by determining the average flow stress and plastic strain ratios [10, 11]. The experiments showed that these were approximately constant from a strain of about 0.005 to diffuse necking. Note that the flow stress ratios in this work are normalized with respect to the flow stress in TD (90° direction). Figure 7 compares the experimental and predicted ratios. As seen from the stress–strain curves, the experimental and predicted flow stress ratios are in good agreement for the 30°, 45° and 75° directions. The predicted plastic strain ratios are also seen to be in good accord with experimental test data for most of the directions: the largest deviations occurred for the 45° and 75° direction and were 68% and 43%, respectively.

An RVE with 8000 grains has a minor effect on the predicted strain hardening (figure 6), average flow stress ratio $\overline{r}_\alpha$ and average plastic strain ratio $\overline{R}_\alpha$ (figure 7). The maximum deviation with respect to the RVE with 1000 grains is about 4%. It can therefore be concluded that a RVE made of 1000 grains is a valid representative volume of the material under study.

5.3. Effect of grain discretization

The results presented in the previous section show the general capability of CP-FEM in reproducing plastic anisotropy for the aluminium alloy studied in this work. A large discrepancy is observed for some directions, however, typically in the ED. In order to identify the weaknesses of the modelling approach, the validity of discretizing the grains as cubic volumes and the influence of the number of elements per grain was assessed. For this purpose, an RVE made of cubic grains discretized with eight elements and a more realistic grain morphology were investigated. For the former, the same assignment of the texture to the
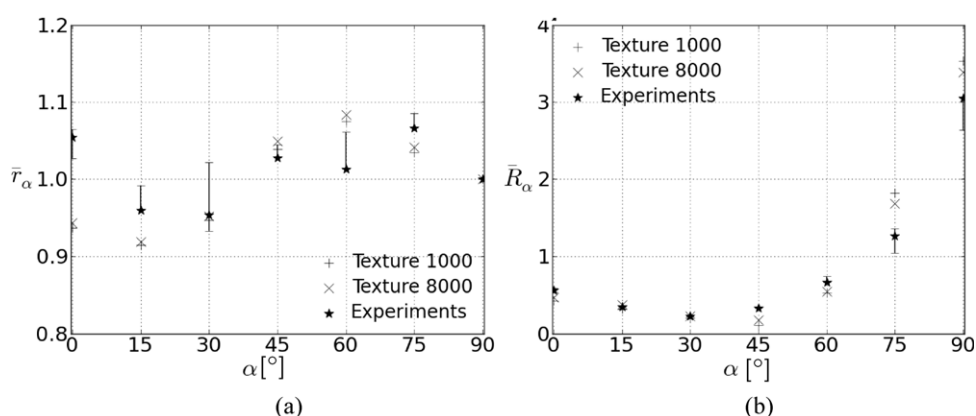
Figure 7. Comparison between experimental and numerical (CP-FEM) (*a*) average flow stress ratio and (*b*) average plastic strain ratio.

grains as 'texture 1000a' was used. For the latter a random periodic microstructure made of 1000 grains was generated using Voronoï tessellation (figure 8) and discretized with 64 000 cubic eight-node elements with eight integration points, i.e. about 64 elements per grain in average. Uniaxial tensile loading in extrusion and transverse directions were carried out using the same boundary conditions and the same texture, i.e. the same grain orientations, as in the previous section. Figure 9 summarizes the responses, in terms of true stress versus true strain curves, obtained for the different spatial discretizations, i.e. one element per grain, eight elements per grain and a finer mesh (64 elements per grain in average), for the extrusion and transverse directions. The stress versus strain curve for the finer mesh is almost identical to the one obtained with eight elements per grain for both directions. Evidently, the more realistic grain morphology gives the same results as the simpler spatial discretizations. This seems to indicate that, for this material, texture is an important source of anisotropy and grain interactions play a negligible role on the macroscopic material response.

Although all RVEs give the same macroscopic true stress versus true strain response, whatever the grain discretization, it is interesting to compare the local strain fields within the RVEs. Figure 10 thus shows the plastic strain field in each RVE. The range of plastic strain as well as the maximum plastic strain within the RVE increases with the number of elements per grain. This shows that a higher number of elements per grain better accounts for the strain gradients within the grains. In contrast, this does not affect markedly the macroscopic response. These results are consistent with a recent study from other authors [46].

In addition to grain discretization, boundary conditions may also affect the results. The methodology followed above was performed once more where periodic boundary conditions were enforced on all faces of the RVE. The obtained true stress versus true strain curves, flow stress and plastic strain ratios were similar to those shown above and are therefore not presented here.

6. Polycrystal modelling

Based on the previous results, i.e. the negligible effect of grain discretization, one may consider using a simpler approach than CP-FEM for modelling the polycrystalline aggregate, for example a model which does not account for grain interactions and grain discretization. For this purpose, two other modelling approaches were investigated; the full-constraint Taylor model
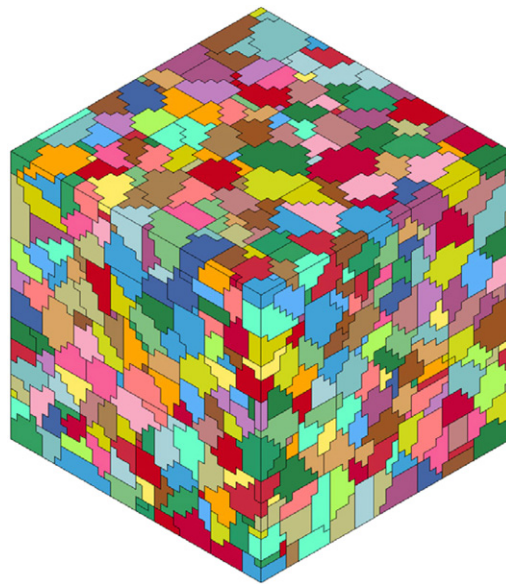
Figure 8. Realistic grain morphology generated using Voronoï tessellation.
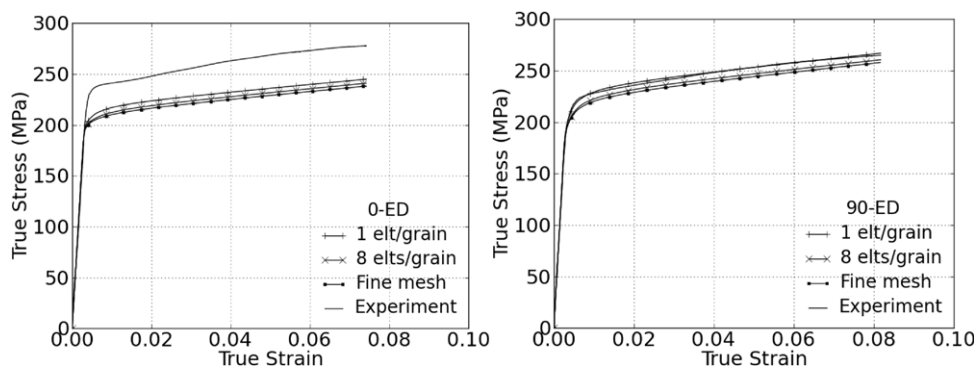

Figure 9. True stress versus true strain curves for 0° and 90° directions: effect of mesh discretization.

[47] and the rigid viscoplastic self-consistent (VPSC) formulation developed by Lebensohn and Tomé [48]. For the former, the same framework as presented in section 2 was used but all grains were assumed to be subjected to the same deformation gradient. This model was also implemented in the commercial finite element code LS-DYNA by use of a user material subroutine (UMAT) [42]. One finite element was used with the same texture as previously presented.

The VPSC model was run as a stand-alone polycrystal plasticity code. In the VPSC formulation, each grain of the polycrystal is treated as an inclusion embedded into and interacting with a homogeneous equivalent medium, the matrix, which has the average properties of the whole aggregate. The properties of the matrix, not known *a priori*, are adjusted in a self-consistent manner so that they coincide with the average properties of the whole aggregate. Unlike the Taylor model, the grains may deform differently depending on their
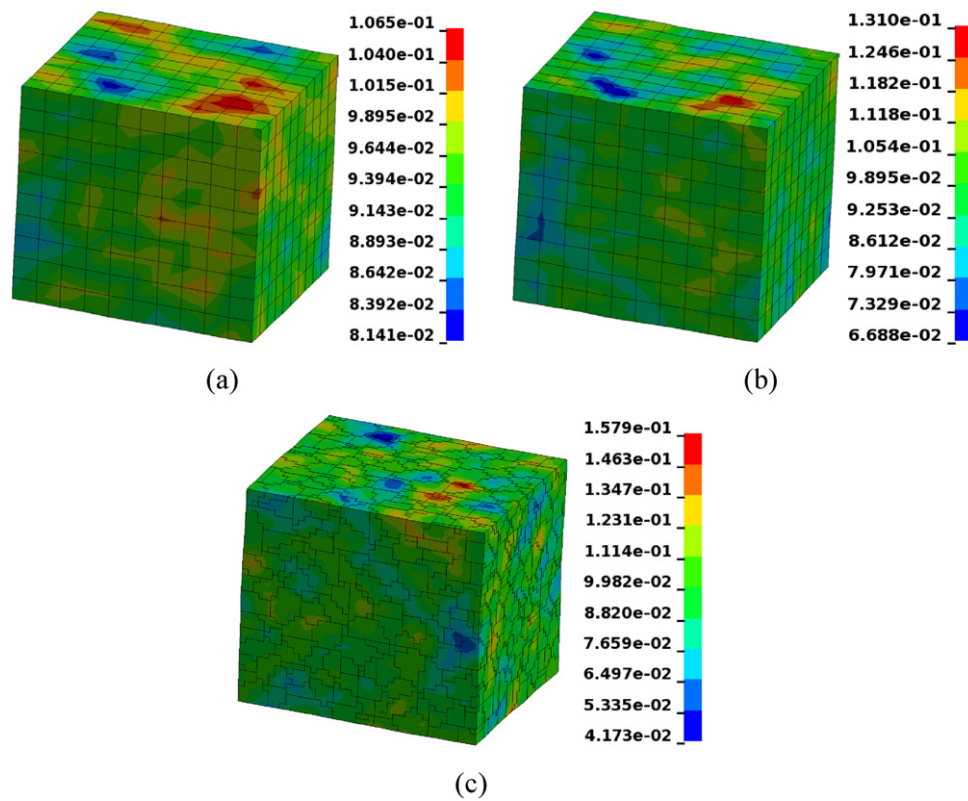
Figure 10. Plastic strain field in RVEs using (*a*) one element per grain, (*b*) eight elements per grain and (*c*) a fine mesh, under uniaxial tensile loading in TD.

relative stiffness with respect to the matrix. The VPSC formulation offers several interaction schemes between matrix and inclusion, and the compliant tangent approach provided the best correlation between experimental and predicted flow stress and plastic strain ratios. Figure 11 shows the true stress versus true strain curves for the different approaches, i.e. CP-FEM, Taylor and VPSC, all compared with the experimental data, for $0°$, $30°$, $60°$ and $90°$ directions. All approaches show similar capabilities except VPSC, which exhibits a lower and a higher deviation for the $0°$ and $30°$ directions, respectively. Figure 12 shows the obtained average flow stress and average plastic strain ratios for plastic strains up to necking. Again, all approaches give similar results. As already noticed above, VPSC predicts a flow stress ratio closer to the experiment for the $0°$ direction, whereas larger deviations are obtained for the $30°$ and $45°$ directions. It is also found that VPSC displays slightly higher hardening rates whatever the direction compared with the other methods.

Finally, the yield surface for the material was computed using each approach, henceforth referred to as CP-based yield surfaces. For CP-FEM and Taylor, the yield surfaces were computed for a plastic work equivalent to 0.2% plastic strain in uniaxial tensile testing along the ED. For VPSC, which is only plastic, the yield surface was computed at yielding. In the VPSC computations, randomly scattered points in the stress space were obtained; about 100 points were generated for CP-FEM and Taylor, and about 1080 for VPSC. These points were then used to calibrate the yield function Yld2004-18p, which was proposed by Barlat *et al* [19]. In the calibration, the exponent was set to 8, as often chosen for fcc materials, while
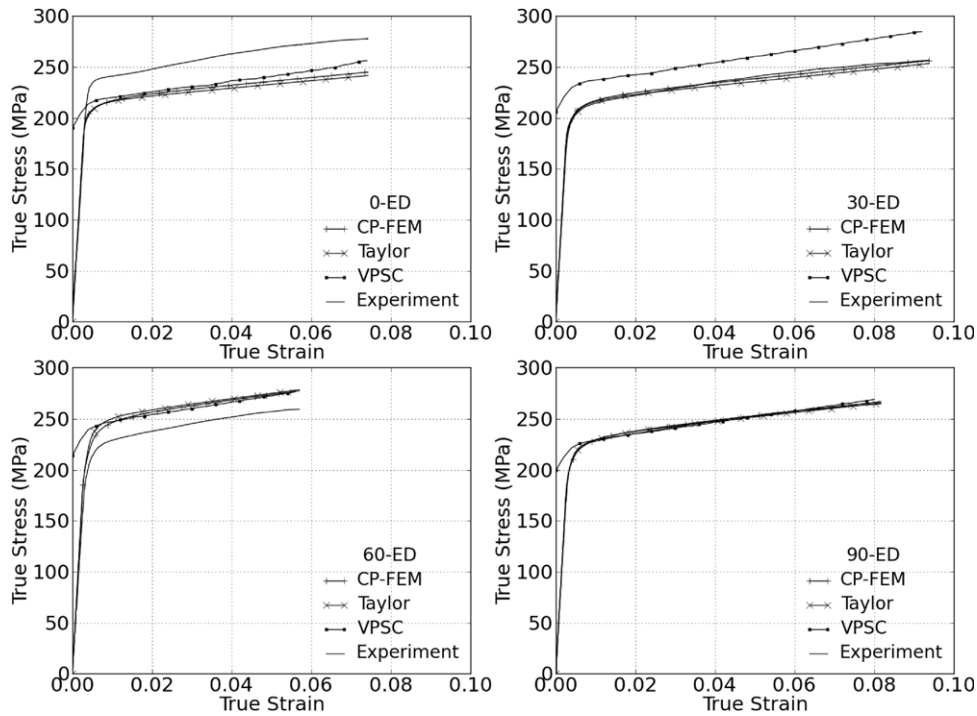
Figure 11. True stress versus true strain curves for 0°, 30°, 60° and 90° directions: comparison between experimental results and simulations for CP-FEM, Taylor and VPSC.
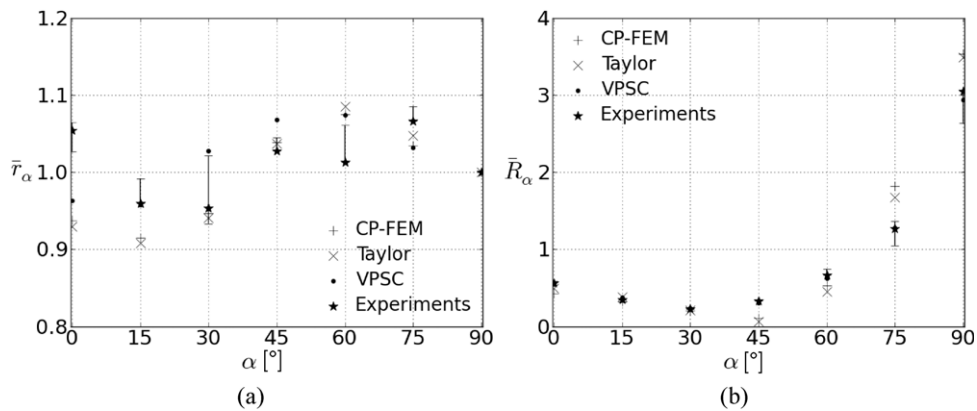
Figure 12. (*a*) Average flow stress ratio and (*b*) average plastic strain ratio: comparison between experimental results and simulations for CP-FEM, Taylor and VPSC. Errors bars corresponding to experimental scatter are also included.

all other coefficients were free. Note that all yield surfaces are normalized such that the flow stress ratio equals unity in the transverse direction. Figure 13 compares the CP-based yield loci with those obtained based on experimental data from Achani *et al* [11] in planes defined by $\sigma_{xy} = 0$ and $\sigma_x = \sigma_y$. The yield surfaces obtained using CP-FEM, Taylor or VPSC are similar, but some differences noted in uniaxial tension in the ED and in equi-biaxial tension are
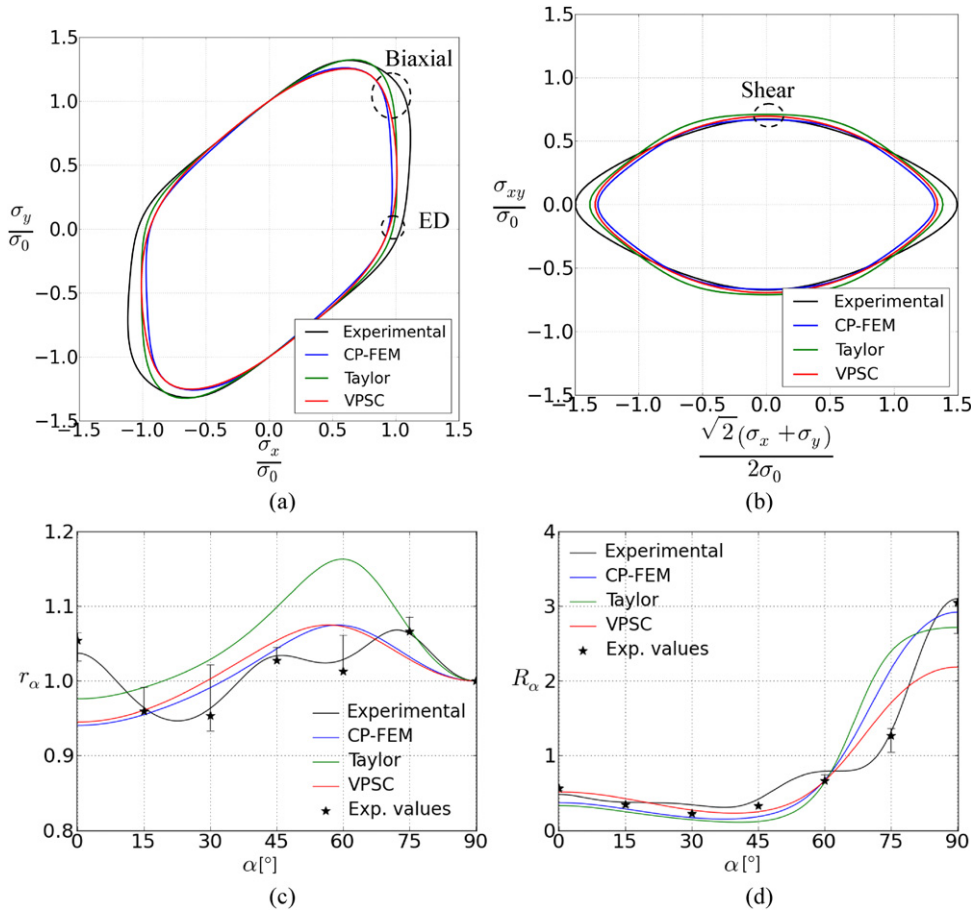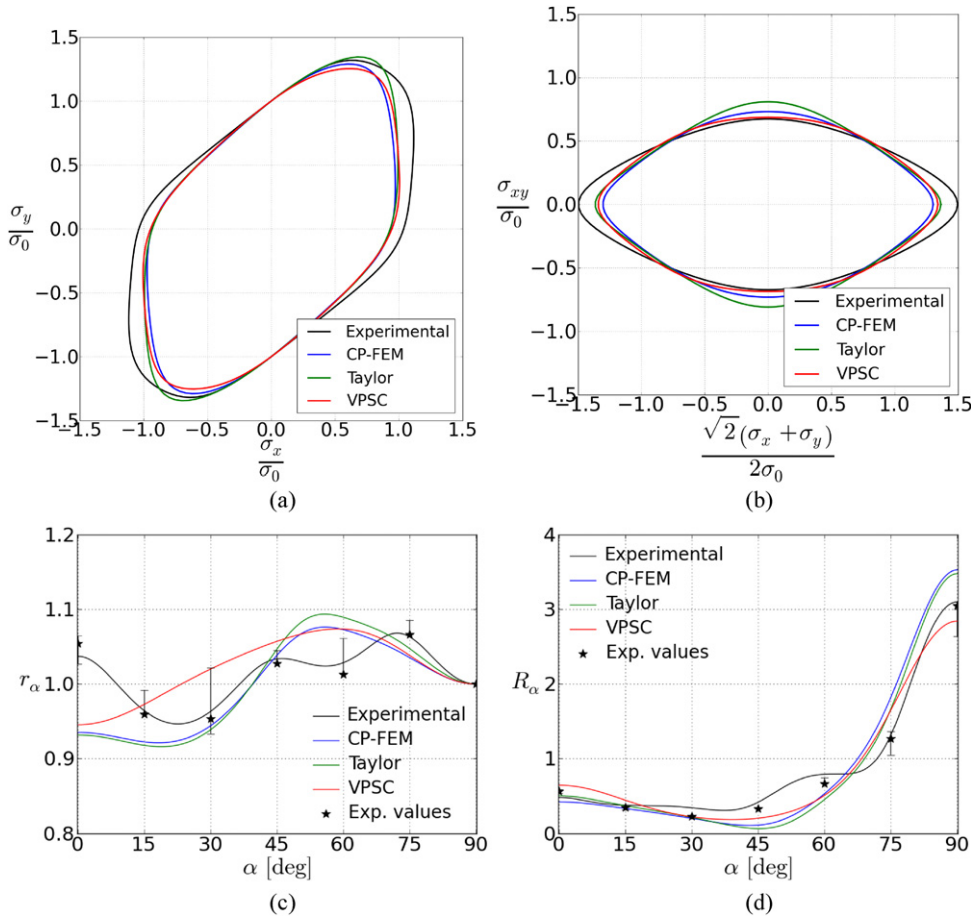
Figure 13. Yield loci in (*a*) $\sigma_{xy} = 0$ plane and (*b*) $\sigma_x = \sigma_y$ plane, (*c*) flow stress ratio and (*d*) plastic strain ratio from Yld2004-18p: comparison between experimental and simulations for CP-FEM, Taylor and VPSC.

highlighted (circles on yield loci in the $\sigma_{xy} = 0$ plane, figure 13). The yield surface predicted by CP-FEM seems to be the sharpest, i.e. less rounded, in the $\sigma_{xy} = 0$ plane but the smoothest, i.e. most rounded, in the $\sigma_x = \sigma_y$ plane. When compared with the yield surface obtained using experimental data [11], the CP-based yield surfaces predict similar stress states in shear (circle on yield loci in the $\sigma_x = \sigma_y$ plane, figure 13). However, notable differences appear in equi-biaxial tension. Nevertheless, it is worth noting that all CP-based yield surfaces correctly predict the stress states around the shear mode.

Comparisons of yield loci only provide insight into parts of the yield surface. To complement the picture, flow stress ratios r_α and plastic strain ratios R_α obtained from the CP-yield surfaces are also shown in figure 13. The flow stress and plastic strain ratios for CP-based, yield surfaces in figure 13 do not reproduce the values seen in figure 12, for angles between $0°$ and $45°$. It is important here to recall that the flow stress ratios in figure 12 were obtained from an average for plastic strains up to necking. On the other hand, in figure 13, these ratios were computed from yield surfaces calibrated against simulations carried out until a given plastic work and under the assumption of isotropic hardening. This indicates that

15

Figure 14. Yield loci in (*a*) $\sigma_{xy} = 0$ plane and (*b*) $\sigma_x = \sigma_y$ plane, (*c*) flow stress ratio and (*d*) plastic strain ratio from Yld2004-18p: comparison between experimental and simulations for CP-FEM, Taylor and VPSC using a weighted calibration.

the flow stress ratios depend on plastic work, although within small variations, and thus that isotropic hardening is not entirely a correct assumption.

A new calibration of the CP-based yield surfaces was performed including average flow stress and average plastic strain ratios for plastic strains up to necking (figure 12). The obtained results were similar to those shown in figure 13. A weight 10 times higher than the one assigned to the CP-based points was then used. The flow stress and plastic strain ratios thus obtained (see figure 14) reproduce the trend seen in figure 12. While no noticeable changes are seen for the yield loci in the $\sigma_{xy} = 0$ plane, an increase in the value for pure shear is observed (compare figure 14 with figure 13).

7. Discussion

This study shows the capability of CP-FEM in describing the plastic anisotropy in extruded AA6063-T6 profiles in terms of directional flow stress and plastic strain ratios. Significant deviations between the experimental data and model predictions were, however, revealed.
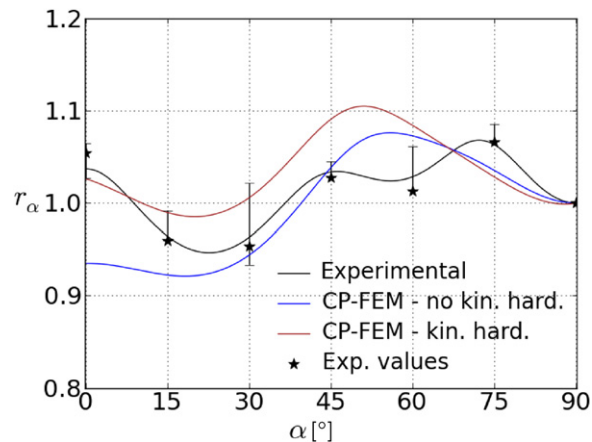
Figure 15. Flow stress ratio from Yld2004-18p: comparison between experimental and simulations for CP-FEM including effect of kinematic hardening. Errors bars corresponding to experimental scatter are also included.

Effects of texture discretization, number of grains and grain discretization were assessed but proved negligible for the specific overall responses investigated in this study. This would probably not be the case for other responses of interest that depend on microscale spatial distribution of local response such as fracture or failure related responses, where the grain interactions would be very important. Finally, CP-FEM was compared with two other polycrystal modelling approaches, namely the full-constraint Taylor and the VPSC formulation. Taylor, VPSC and CP-FEM describe interactions between grains and their neighbours in different ways. It was found that the three methods produced similar results. This indicates that, for this material, texture plays a more important role with respect to plastic anisotropy than interactions between grains. All approaches suffer the same weaknesses, with inaccurate reproduction of the experimental results. Several sources of error can be identified.

Firstly, the history of the material is ignored. It has implicitly been assumed that all slip systems in the polycrystal have the same initial slip resistance, which is a reasonable assumption for annealed materials but not for work-hardened materials. The material in question has been extruded followed by 0.5% to 1% stretching, cutting and tempering, resulting in inhomogeneous slip activity on the different slip systems and thereby slip resistance. Furthermore, the deformation structure, characterized by dense dislocation walls and microbands, which contribute to both resistance to slip and anisotropy [49, 50], is not described by the modelling approach used in this study but might be significant.

Other causes for directional dependence could be attributed to kinematic hardening effects that are not accounted for in the above approach. Such effects may play a significant role [51]. The effect of kinematic hardening caused by profile levelling/stretching on the predicted anisotropy in uniaxial tension is assessed here in the following way: (i) the shape of the yield surface was assumed to be defined by the texture, using CP-FEM, which is not affected by stretching since the strains are small, (ii) a back stress tensor with three components was included in the yield function (this study only deals with flat profiles) and (iii) the back stress components were calibrated against the experimental values for average flow stress ratios. The obtained results are shown in figure 15 together with the experimental values for average flow stress ratios and error bars. Note that the size of the yield surface was changed so that the flow stress in the 90° direction was kept equal to unity. A better description of the flow stress

ratio is obtained for orientations between 0° and 15°; the values at 15° and 30° have increased but are still within the experimental scatter and only a small decrease is observed between 65° and 90°. However, for the other directions, the deviation from the experimental results has increased. Nevertheless, the flow stress ratio at 0° is improved and the calibration shows that the back stress component with highest value is the one along the ED, which is consistent with the experimental facts, i.e. stretching along the ED.

Secondly, as figure 1 shows, and as extensively described by other authors [42, 52, 53], microstructure and texture gradients are present through the thickness. The centre has a strong cube texture, which gradually changes into a combination of Goss and cube components before becoming more random close to the surface. These variations are not accounted for in this study while their effect might be important [54]. In addition, the different texture components were randomly placed spatially in the microstructure, i.e. no spatial correlation, such as the misorientation distribution function (MDF), was accounted for. This assumption might affect the material response, since different spatial placements of the same texture components may generate different responses, as observed for example in the case of roping [55].

Finally, effect of constituent particles, rich in iron, may also play a role. During extrusion, these particles break up and become aligned with the ED; then, after extrusion, the material is stretched along the ED. These processing steps might generate a directional effect of the constituent particles.

8. Conclusions

Plastic anisotropy in aluminium alloy AA6063-T6 was described using the crystal plasticity finite element method. A rate-dependent constitutive model with a Voce-type hardening law was used at the crystal level. The material was modelled using a representative volume element made of 1000 grains with periodic boundary conditions and a reduced texture selected from experimental measurements. The model parameters were obtained using uniaxial tensile data in the transverse direction of the extrusion. True stress versus true strain curves in seven directions between extrusion and transverse directions were predicted and compared with the experimental results. The predicted directional dependence of flow stress and plastic strain ratios were in general in reasonable agreement with experiments. However, significant deviations were disclosed in some directions indicating there are other sources to the plastic anisotropy than crystallographic texture. Effects of grain discretization, grain shape and boundary conditions were assessed to identify weaknesses in the approach. However, no noticeable effects were observed for the abovementioned macroscopic responses investigated in this study. Approaches using one or eight elements per grain, realistic grain shape and size distribution, or alternative polycrystal plasticity approaches such as FC-Taylor or VPSC all led to similar results. The weaknesses of the modelling approach were then attributed to prior material history originating from product processing, such as material inhomogeneity and kinematic hardening and representation of the texture. Further work will be undertaken to assess the effect of the identified weaknesses and eventually to account for them.

References

[1] Engler O and Hirsch J 2002 Texture control by thermomechanical processing of AA6xxx Al–Mg–Si sheet alloys for automotive applications—a review *Mater. Sci. Eng.* **336** 249–62

[2] Fjeldly A and Roven H J 1996 Observations and calculations on mechanical anisotropy and plastic flow of an AlZnMg extrusion *Acta Mater.* **44** 3497–504

[3] Fjeldly A and Roven H J 1997 Phenomenological modeling of the mechanical anisotropy in AlZnMg extruded profiles *Mater. Sci. Eng.* A **234–236** 606–9

[4] Hopperstad O S, Langseth M and Remseth S 1995 Cyclic stress–strain behaviour of alloy AA 6060 T4: II. Biaxial experiments and modelling *Int. J. Plast.* **11** 741–62

[5] Lademo O-G, Hopperstad O S and Langseth M 1999 An evaluation of yield criteria and flow rules for aluminium alloys *Int. J. Plast.* **15** 191–208

[6] Lademo O-G, Hopperstad O S, Malo K A and Pedersen K O 2002 Modelling of plastic anisotropy in heat-treated aluminium extrusions *J. Mater. Process. Technol.* **125–126** 84–8

[7] Lademo O-G, Hopperstad O S, Berstad T and Langseth M 2005 Prediction of plastic instability in extruded aluminium alloys using shell analysis and a coupled model of elasto-plasticity and damage *J. Mater. Process. Technol.* **166** 247–55

[8] Li S, Engler O and Van Houtte P 2005 Plastic anisotropy and texture evolution during tensile testing of extruded aluminium profiles *Modelling Simul. Mater. Sci. Eng.* **13** 783–95

[9] Reyes A, Hopperstad O S, Lademo O-G and Langseth M 2006 Modeling of textured aluminium alloys used in a bumper system: Material tests and characterization *Comput. Mater. Sci.* **37** 246–68

[10] Achani D, Hopperstad O S and Lademo O-G 2009 Behaviour of extruded aluminium alloys under proportional and non-proportional strain paths *J. Mater. Proc. Technol.* **209** 4750–64

[11] Achani D, Lademo O-G, Engler O and Hopperstad O S 2011 Evaluation of constitutive models for textured aluminium alloys using plane-strain tension and shear tests *Int. J. Mater. Form.* **4** 227–41

[12] Hill R 1948 A theory of the yielding and plastic flow of anisotropic metals *Proc. R. Soc. Lond.* A **193** 281–97

[13] Barlat F, Lege D J and Brem J C 1991 A six-component yield function for anisotropic materials *Int. J. Plast.* **7** 693–712

[14] Barlat F *et al* 1997 Yield function development for aluminium alloy sheets *J. Mech. Phys. Solids* **45** 1727–63

[15] Barlat F, Brem J C, Yoon J W, Chung K, Dick R E, Lege D J, Pourboghrat F, Choi S H and Chu E 2003 Plane stress yield function for aluminium alloy sheets: I. Theory *Int. J. Plast.* **19** 1297–319

[16] Banabic D, Kuwabara T, Balan T, Comsa D S and Julean D 2003 Non-quadratic yield criterion for orthotropic sheet metals under plane-stress conditions *Int. J. Mech. Sci.* **45** 797–811

[17] Cazacu O and Barlat F 2003 Application of the theory of representation to describe yielding of anisotropic aluminium alloys *Int. J. Eng. Sci.* **41** 1367–85

[18] Aretz H 2005 A non-quadratic plane stress yield function for orthotropic sheet metals *J. Mater. Proc. Technol.* **168** 1–9

[19] Barlat F, Aretz H, Yoon J W, Karabin M E, Brem J C and Dick R E 2005 Linear transformation based anisotropic yield functions *Int. J. Plast.* **21** 1009–39

[20] Anand L 1985 Constitutive equations for hot-working of metals *Int. J. Plast.* **1** 213–31

[21] Anand L and Kothari M 1996 A computational procedure for rate-independent crystal plasticity *J. Mech. Phys. Solids* **44** 525–58

[22] Peirce D, Asaro R J and Needleman A 1982 An analysis of nonuniform and localized deformation in ductile single crystals *Acta Metall.* **30** 1087–119

[23] Cuitiño A and Ortiz M 1993 Computational modelling of single crystals *Modelling Simul. Mater. Sci. Eng.* **1** 225–63

[24] Kalidindi S R, Bronkhorst C A and Anand L 1992 Crystallographic texture evolution in bulk deformation processing of fcc metals *J. Mech. Phys. Solids* **40** 537–69

[25] Tabourot L, Dumoulin S and Balland P 2001 An attempt for a unified description from dislocation dynamics to metallic plastic behaviour *J. Phys. IV* **11** Pr5-111–8

[26] Grujicic M and Batchu S 2002 Crystal plasticity analysis of earing in deep-drawn OFHC copper cups *J. Mater. Sci.* **37** 753–64

[27] Zhao Z, Kuchnicki S, Radovitzky R and Cuitiño A 2007 Influence of in-grain mesh resolution on the prediction of deformation textures in fcc polycrystals by crystal plasticity FEM *Acta Mater.* **55** 2361–73

[28] Prakash A, Weygand S M and Riedel H 2009 Modeling the evolution of texture and grain shape in Mg alloy AZ31 using the crystal plasticity finite element method *Comput. Mater. Sci.* **45** 744–50

[29] Alankar A, Mastorakos I N and Field D P 2009 A dislocation-density-based 3D crystal plasticity model for pure aluminum *Acta Mater.* **57** 5936–46

[30] Inal K, Mishra R K and Cazacu O 2010 Forming simulation of aluminum sheets using an anisotropic yield function coupled with crystal plasticity theory *Int. J. Solids Struct.* **47** 2223–33

[31] Watanabe I and Terada K 2010 A method of predicting macroscopic yield strength of polycrystalline metals subjected to plastic forming by micro–macro de-coupling scheme *Int. J. Mech. Sci.* **52** 343–55

[32] Roters F, Eisenlohr P, Hantcherli L, Tjahjanto D D, Bieler T R and Raabe D 2010 Overview of constitutive laws, kinematics, homogenization and multiscale methods in crystal plasticity finite-element modeling: theory, experiments, applications *Acta Mater.* **58** 1152–211

[33] Van Houtte P, Li S, Seefeldt M and Delannay L 2005 Deformation texture prediction: from the Taylor model to the advanced Lamel model *Int. J. Plast.* **21** 589–624

[34] Van Houtte P, Kanjarla A K, Van Bael A, Seefeldt M and Delannay L 2006 Multiscale modelling of the plastic anisotropy and deformation texture of polycrystalline materials *Eur. J. Mech.* A **25** 634–48

[35] Lee E H and Liu D T 1967 Finite-strain elastic–plastic theory with application to plane-wave analysis *J. Appl. Phys.* **38** 19–27

[36] Mandel J 1973 Equations constitutives et directeurs dans les milieux plastiques et viscoplastiques *Int. J. Solids Struct.* **9** 725–40

[37] Rice J R 1971 Inelastic constitutive relations for solids: an internal variable theory and its application to metal plasticity *J. Mech. Phys. Solids* **19** 433–55

[38] Voce E 1948 The relationship between stress and strain for homogeneous deformation *J. Inst. Met.* **74** 537–62

[39] Tomé C, Canova G R, Kocks U F, Christodoulou N and Jonas J J 1984 The relation between macroscopic and microscopic strain hardening in F.C.C. polycrystals *Acta Metall.* **32** 1637–53

[40] Estrin Y 1998 Dislocation theory based constitutive modelling: foundations and applications *J. Mater. Process. Technol.* **80–81** 33–9

[41] Hallquist J O 2007 *LS-DYNA Keyword User's Manual* Version 971 (California: Livermore Software Technology Corporation)

[42] Dumoulin S, Hopperstad O S and Berstad T 2009 Investigation of integration algorithms for rate-dependent crystal plasticity using explicit finite element codes *Comput. Mater. Sci.* **46** 785–99

[43] Fjeldbo S K 2004 Study of texture and microstructure gradients in extruded aluminium profiles of AA6063 and AA6082 (in Norwegian) *Master Thesis* Norwegian University of Science and Technology, Trondheim, Norway

[44] Lequeu P, Gilormini P, Montheillet F, Bacroix B and Jonas J J 1987 Yield surfaces for textured polycrystals-I, crystallographic approach *Acta Metall.* **35** 439–51

[45] Stander N, Roux W, Goel T, Eggleston T and Craig K 2010 *LS-OPT User's Manual* Version 4.1 (California: Livermore Software Technology Corporation)

[46] Tadano Y, Kuroda M and Noguchi H 2012 Quantitative re-examination of Taylor model for FCC polycrystals *Comput. Mater. Sci.* **51** 290–301

[47] Taylor G I 1938 Plastic strain in metals *J. Inst. Met.* **62** 307–24

[48] Lebensohn R A and Tomé C N 1993 A self-consistent anisotropic approach for the simulation of plastic deformation and texture development of polycrystals: application to zirconium alloys *Acta Metall. Mater.* **41** 2611–24

[49] Juul Jensen D and Hansen N 1990 Flow stress anisotropy in aluminium *Acta Metall. Mater.* **38** 1369–80

[50] Hansen N and Juul Jensen D 1992 Flow stress anisotropy caused by geometrically necessary boundaries *Acta Metall. Mater.* **40** 3265–75

[51] Kalidindi S R and Schoenfeld S E 2000 On the prediction of yield surfaces by the crystal plasticity models for fcc polycrystals *Mater. Sci. Eng.* A **293** 120–9

[52] Bjerkaas H 2007 Characterisation and plasticity in extruded Al–Mg–Si profiles engaging *in-situ* EBSD *PhD Thesis* Norwegian University of Science and Technology, Trondheim, Norway

[53] Fjeldbo S K 2008 Studies of the influence of strong through thickness texture variation on the plastic flow properties of extruded AA6063-W aluminium strips and tubes, with application to the modelling and simulation of tube hydroforming of T-shapes *PhD Thesis*, Norwegian University of Science and Technology, Trondheim, Norway

[54] Van Bael A, Hoferlin E, Kestens L and Van Houtte P 1998 Side-bulging during tensile tests of IF-steels with cross-thickness texture gradients *Mater. Sci. Forum* **273–275** 417–22

[55] Zhao Z, Radovitzky R and Cuitiño A 2004 A study of surface roughening in fcc metals using direct numerical simulation *Acta Mater.* **52** 5791–804

20